

Realization of Lattice Formation in Nonlinear Two-dimensional Potential by Mobile Robots

Yanran Wang Tatsuya Baba Takashi Hikiyara
Department of Electrical Engineering, Kyoto University

May 10, 2022

Abstract

Formation control in multi-agent system has earned significant research interests in both theoretical aspect and applications over the past two decades. However, the study on how the external environment shapes swarm formation dynamics, and the design of formation control algorithm for multi-agent system in nonlinear external potential have not been rigorously investigated. In this paper, we present a formation control algorithm for mobile robots travelling in nonlinear external potential. Experiments are performed on real mobile robots to verify the algorithm, and the effectiveness of Dynamical Mode Decomposition in robot's velocity prediction in unknown environment is demonstrated.

1 Introduction

Multi-agent systems (MAS) are systems where the global objective is accomplished by the local interactions among a group of simple agents. In the field of swarm robotics, researchers try to formulate and understand existing MAS in nature, such as birds flocking, in terms of dynamical systems [1, 10, 19, 21, 24, 35], or construct MAS using artificial robots that is useful in a wide range of applications [6, 20, 23, 28, 40]. Due to the constraint of the complexity of individuals in MAS, agent acts autonomously based on only local perception and coordination with its neighbours. At the same time, with limited sensing and communication capabilities, MAS naturally maintains formation as a group.

Swarm formation is often observed in natural MAS, and have inspired researchers to develop algorithms which can perform formation control on artificial swarms. Recent advances in swarm robotics have presented various successful implementations of swarm formation control for both centralized and decentralized approaches. However, these swarm formation control are generally studied as a standalone problem [3, 24, 27, 34, 35, 38]. Researches are focused on how to maintain formation when facing obstacles in the environment, while not much attention is paid to the formation dynamics shaped by environments. On the other hand, when swarm robotics applied in unknown environment mapping

tasks [15, 25], swarm formation appears only as a byproduct of maximizing coverage area while maintain agent-to-agent connections.

In the previous study [36], we have formulated algorithms where desired environmental information is obtained through analyzing the change in sensor swarm formations, rather than information collected directly through individual sensors. We identify the environmental information as an external potential hyperspace M of $(n - 1)$ -dimensions. The swarm formation is defined using the geodesic deviation equation. To maintain the defined swarm formation, Koopman operator theory [4, 22, 32] and Dynamic Mode Decomposition (DMD) [39] are used to predict the state of the nonlinear autonomous dynamical system of individual agents in the swarm.

In this study, experiment is performed to verify the designed algorithms for formation control. Two omnidirectional mobile robots, one leader and one follower, equipped with visual system and sensing system are experimented on an elliptic paraboloid potential. Visual algorithm and velocity prediction algorithm are designed, which allows the robots to maintain defined lattice formation in travelling on nonlinear external potential. The formation control algorithm is easily scalable to include more follower robots in the formation.

This paper is organized as the follows. Section 2 gives a brief survey of related work. In Section 3, we introduce the mathematical definition of the lattice formation and demonstrate how to construct such formation in an arbitrary external potential both in theory and in experiment. For Section 4, we explain the experimental setups, including specification of the external potential, and the hardware specifications of the mobile robot. In Section 5, we formulate the algorithm which guides the individual robot to stay in lattice formation as it moves in the external potential. Section 6 we present and discuss on the experimental results with mobile robots. Finally, Section 7 concludes the paper.

2 Related Work

In this section, we provide a brief survey of related work with focuses on swarm formation control algorithms. Formation control of multi-agent systems has been studied by researchers with backgrounds in control theory, computer science, biology, and physics. Two of the main focusing area is understanding and modelling of natural MAS, such as bird flocking, and swarm engineering with the goal of designing predictable, controllable swarms with well-defined global goals and provable minimal conditions [14].

There are different strategies towards swarm formation control. Three strategies are discussed in this section: behaviour-based method, virtual structure method, and leader-follower method.

The behaviour-based approach mainly consists of several sub-behaviours including moving to the goal, avoiding obstacles, wall-following, avoiding robot, and formation keeping [2]. In this method, the trajectories of each robot is considered as a time series of asymptotically stable system states. The overall formation control is achieved by the stability of individual robots in the

swarm. This method is often used for swarm robotic applications of navigation in an unknown environment with obstacles. Many researchers have successfully demonstrated swarm formation control using this method [2, 9, 13, 27, 31, 37]. The mathematical analysis of this method is complicated, and the guarantee for the stability of desired formation, especially in complex environments, is difficult to obtain [5, 37].

In the virtual structure method, the entire formation is considered as a single rigid body. The positions of the robots in the swarm are defined with respect to a reference point in the structure. As the trajectory for the reference point is predefined, the desired trajectory for each robot is calculated as the rigid body evolves in time [12, 16, 18, 26, 33]. The main advantages of this approach is that a single mathematical rule governs the robot's behavior. The method is not suitable for applications where the trajectory of the reference point is unknown, and formation change as time evolves is also difficult to realize.

In leader-follower method, the swarm is divided into two categories: leader and follower. The leader robot is designed to travel along a predefined trajectory, while the follower robots are to maintain a fixed relative distance with respect to the designated neighbouring robot [7, 29, 30]. This method is more suitable for environments without obstacles, and situations where robots are initially localized near the desired formation.

Our proposed formation control algorithm can be categorized into leader-follower method. Our approach is decentralized, and mainly focused on how the follower robot maintain desired formation in nonlinear external potential efficiently. To the best of our knowledge, Koopman theory and DMD are first used in leader-follower formation control algorithm for swarm robots to provided trajectory predictions.

3 Methodology

3.1 Lattice formation

The topology of the lattice formation follows [36], which is line formation. Mathematically, we define a *path graph* P_n as a pair $(\mathcal{V}, \mathcal{E})$ that consists of a set of vertices $\mathcal{V} = \{v_1, v_2, \dots, v_n\}$ and a set of edges \mathcal{E} such that $\mathcal{E} \subseteq \{v_i, v_{i+1}\}$, where $i = 1, 2, \dots, n-1$. Each vertex represents an individual robot, while the edges represent the distance between any two neighbouring robots. To define the edges unambiguously, let $q = (q_1, \dots, q_n)^T$ be the configuration of all robots, where $q_i \in \mathbb{R}$ denote the position of robot v_i for all $v_i \in \mathcal{V}$. The length of edges, $dis(\mathcal{E})$, is defined to be the geodesic distance between two connected vertices over $G(q)$.

To stay in lattice formation, all robots are to maintain an identical inter-robot distance. Thus we force an algebraic constraint on the edges,

$$dis(\mathcal{E}_{v_i, v_{i+1}}) = d, \quad \forall v_i \in V, \quad d \in \mathbb{R}. \quad (1)$$

The robots are being separated into two types, leader and followers. The

leader robot has a predefined trajectory, which acts as the initial stimulus for the whole formation. The followers takes its neighbour as beacon robot (whichever is closer to the leader robot), and keep constant relative distance with this neighbouring robot.

In flat space, or mathematically in \mathbb{R}^2 , the relative distance between each pair of robots is measured along the line that is normal to the velocity of the beacon robot in Euclidean metric. Naturally, observed from the ambient space \mathbb{R}^3 , the lattice formation is a moving straight line that is normal to the velocity of the head robot at each given timesteps, with each follower robots keeping identical relative Euclidean distances. Consequently, the trajectories of the follower robots are to be parallel lines to the leader robot.

In curved space, or mathematically in any arbitrary external potential M , by definition, the edge representation of the lattice formation is a parallel vector field that is metrically orthogonal to the head agent trajectory, with each follower robots separated by identical proper time. Since the edges are metric-dependent, observed from the ambient space \mathbb{R}^3 , the trajectories of the follower robots are no longer parallel to the leader robots.

3.2 Problem Formulation

3.2.1 Mathematical construction of lattice formation

Given the trajectory of leader robot, the trajectory of the follower robot can be constructed base on the definition of lattice formation [11, 17].

We predefine the trajectory of the leader robot to be a geodesic curve on manifold. Eventhough any arbitrary trajectory can be used, this choice of leader robot trajectory is made to simplify its dynamic control. On the geodesic, the leader robot is traveling with constant velocity given initial position and velocity, thus no requirement for outside reference beacon. For a two-dimensional manifold (M, g) , leader robot trajectory $l(t)$ can be expressed as a system of ordinary differential equations

$$\begin{aligned} \dot{l}_1 &= l_3, \\ \dot{l}_2 &= l_4, \\ \dot{l}_3 &= -\Gamma_{\mu\mu}^{\mu}(l_3)^2 - 2\Gamma_{\mu\nu}^{\mu}l_3l_4 - \Gamma_{\nu\nu}^{\mu}(l_4)^2, \\ \dot{l}_4 &= -\Gamma_{\mu\mu}^{\nu}(l_3)^2 - 2\Gamma_{\mu\nu}^{\nu}l_3l_4 - \Gamma_{\nu\nu}^{\nu}(l_4)^2, \end{aligned} \tag{2}$$

where basis $\{\mu, \nu\}$ are used in the index, \dot{l} are the first derivative with respect to time, and Γ are the Christoffel symbols. (See section A for mathematical details)

The distance of the edges of lattice formation needs to be identical in terms of the potential metric. For edges representation, a parallel vector field K that is orthogonal to the leader robot trajectory $l(t)$ is constructed as

$$\nabla_K K = 0. \tag{3}$$

K forms a family of geodesics where the initial position and velocity conditions (u_0^j, v_0^j) for j th geodesic $\gamma_j \in K$ are $u_0^j = l(t_j)$, $v_0^j = v$, such that $g(v, \dot{l}(t_j)) = 0$, $j \in \mathbb{Z}$.

The separation vector $s(t)$ connects a point $\gamma(t)$ on one geodesic to a point $\gamma(t) + s(t)$ on a nearby geodesic at the same proper time. For parallel vector field K , we can construct a separation vector field S such that $s \in S$ are the separation vector described above. The follower robots' trajectories are the integral curves of S .

3.2.2 Experimental construction of lattice formation

The leader robot is defined to travel on geodesic. To have the leader robot traveling in constant speed, we require it to maintain a preset wheel rotation for all four wheels in each given timestep.

The follower robot's trajectory stated in section 3.2.1 requires the knowledge of the metric of the arbitrary potential M . In experiment, this metric is unknown to all the robots. We assume, the inter-robot distance can be measured in Euclidean metric, locally. Therefore, we require the follower robot to be able to detect its relative distance and angle to its beacon neighbour.

Unlike mathematical construction, robots are no longer point-elements. In the experiment, robot-to-robot relative angle and position, and robot's velocity per movement uses the center point of robot as reference point as shown in Fig. 1.

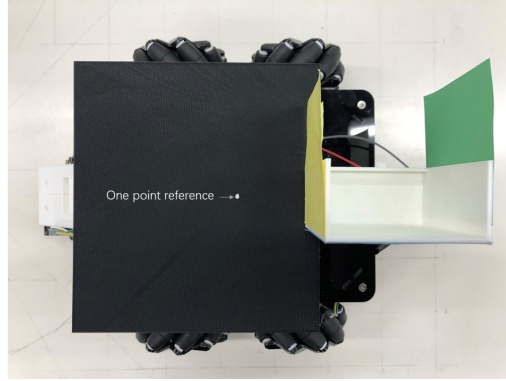


Figure 1: Robot with body cover. The white dot is set as the one-point position reference for the robot.

4 Hardware Design

4.1 Design of external potential

We choose the external potential M to be a two-dimensional elliptic paraboloid, which can be explicitly represented as $\frac{1}{40000}(x_1^2 + x_2^2) - x_3^2 = 0$. Fig. 2 shows a photo of the external potential. A fence cover is build around the potential to reduce interferences for the robots' visual system.

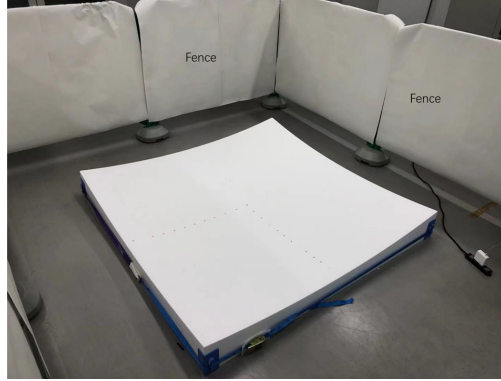


Figure 2: External potential view. The potential is made of polystyrene foam. It is 1780mm by 1780mm, with minimal height 50mm, and maximum height 208.4mm. See section B for more specification of the potential.

4.2 Design of robot

The external view of the robot is shown in Fig. 3. The robot is modified based on OSOYOO® Model ZZ012318MC Metal Chassis Mecanum Wheel. It is 365mm in length, 238mm in width, 216mm in height, and weighs 1700 grams. We define the longer side to be the v-axis of the robot, while the shorter side is the u-axis. Besides the metal and acrylic skeletons, the robot has three main system: movement system, sensing and storage system, and visual system, all connects to the central processing unit, Arduino Due. A body cover is made to reduce the interference for the visual system, and also acts as a one-point reference for the observer as shown in Fig. 1.

4.2.1 Movement system

The movement system is responsible for robot's mobility. The system consists of OSOYOO® Model-X Motor Driver Module, 18650 battery, DC encoder motor, and Mecanum wheels.

Driver module The OSOYOO® Model-X motor driver module is an improved L298N module. Two motor driver modules are used to control the front

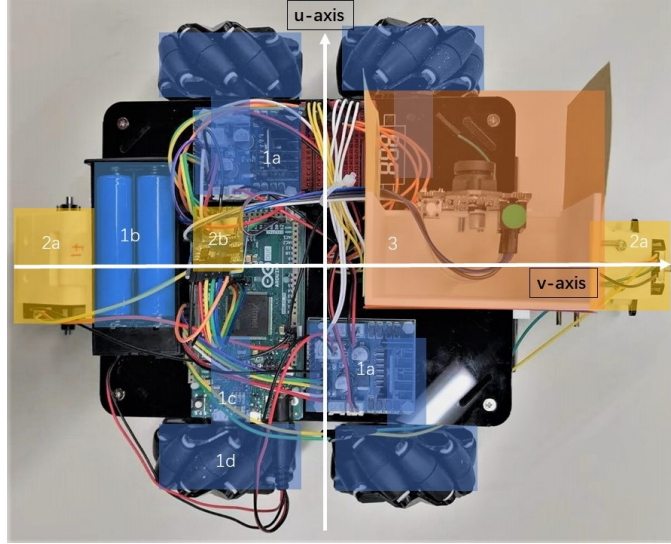


Figure 3: Robot external view. Movement system, sensing and storage system, and visual system are labeled in blue, yellow and orange, respectively. Numerical label indicates respective Section for parts descriptions.

wheels and the rear wheels, respectively.

18650 battery The pair of battery acts as the power supply for the whole robot.

DC encoder motor There are four DC encoder motors, corresponding to the four wheels. Each motor consists of two part, GM25 DC motor and a dual channel encoder. The dual channel encoder can measure wheel rotations of the robot. In this sense, the robot can be programmed to travel a preset distance by giving number of wheel rotations.

Mecanum wheel The Mecanum wheel is an omnidirectional wheel, made with various rubberized rollers obliquely attaching to the wheel rim [8]. With a combination of different wheel driving direction, movements to various directions can be performed. Fig. 4 demonstrates the relationship between wheel rotation directions and robot moving directions.

In ideal condition, all robots would have the same wheel rotation to distance conversion function. However, with the instability and limited accuracy of motors, this conversion function varies for individual robot. To rectify, both leader and follower robots are calibrated by its own distance versus wheel rotation function, as shown in Fig. 5. The motor calibration function is obtained by curve fit the travelled distance measured by observer using one-point reference for various wheel rotations. With the restriction of the size of the external

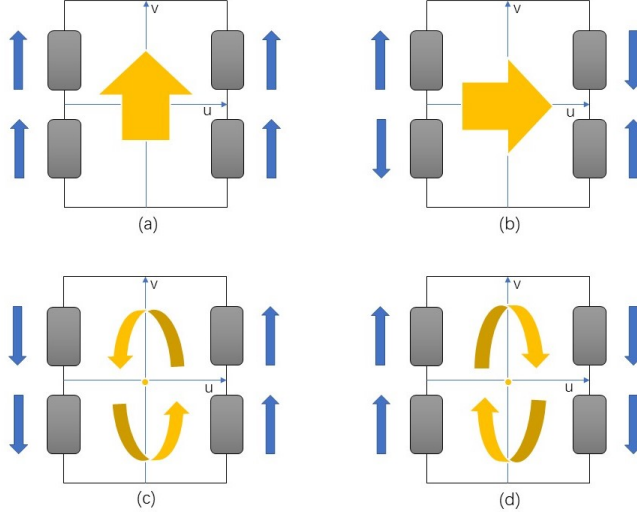


Figure 4: The movement scheme of robot. Blue arrow represents the rotation direction of the wheels, yellow arrow represents movement direction of the robot. Four types of movement are used in the experiment: (a) along v -axis of robot. (b) along u -axis of robot. (c) counterclockwise rotation. (d) clockwise rotation.

potential and the size of robots, we have focused on finetuning the robots with travelling distance under 20 cm along v -axis, and 10 cm along u -axis. Note the leader robot only calibrated for movement along v -axis, since it only requires to travel in that direction.

4.2.2 Sensing and storage system

The sensing and storage system is responsible for measuring and recording robot's velocity (per given timesteps) along its u and v axis.

Sensing system The sensing system is illustrated in Fig. 6.

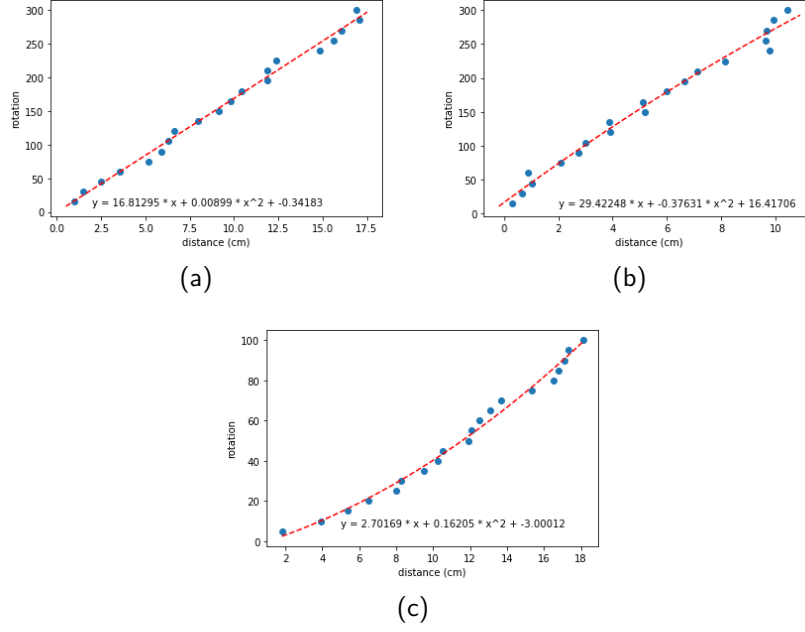


Figure 5: Motor calibration functions. (a) Movement along v-axis for follower robot. (b) Movement along u-axis for follower robot. (c) Movement along v-axis for leader robot.

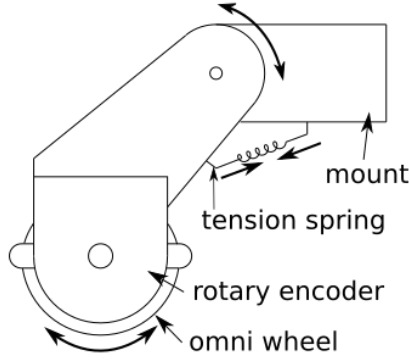


Figure 6: Scheme of robot's sensing system. The sensing system is mounted on the robot's metal skeleton through its supporting platform. The tension spring allows the omni wheel to keep in contact with the potential surface while travelling.

The system is implemented for both v-axis and u-axis. It consists of supporting platform, AMT102-V encoder with configuration 512 resolution and 15000

maximum RPM, and 38mm double aluminum omni wheel. This system is needed to improve the accuracy of velocity measurement, since the encoder on the DC motor is affected by the swiping motion of the robot. Fig. 7 demonstrates the travelled distance measured by sensing system, and by observer using one-point reference for different travelling distance. The sensing system has provided reliable data for the actual velocities of the robot, which is crucial for the velocity prediction algorithm in section 5.3.

Storage system We use a SD card module and 8GB SD card to collect robot's data, such as velocity, current timesteps, and number of movements. However, the storage system is solely for the experimental data analysis. The lattice formation algorithm of the robots does not require such data collection.

4.2.3 Visual system

The visual system consisting Pixy2 Camera with supporting pillar and square color papers, as shown in Fig. 8. The square color papers are of side length 70 mm, and are in three different colors, named front, rear and target color signature.

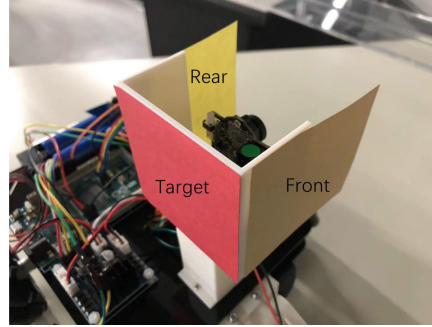
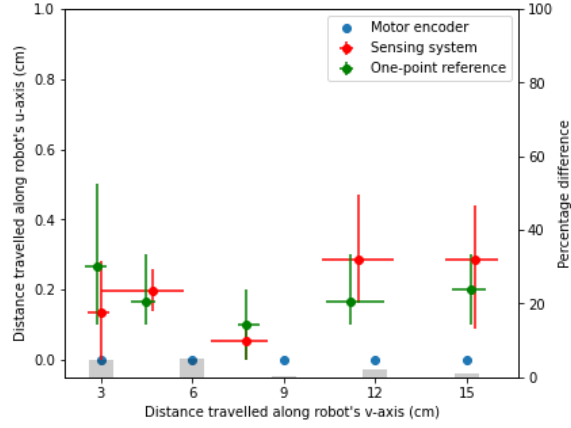


Figure 8: View of the robot's visual system.

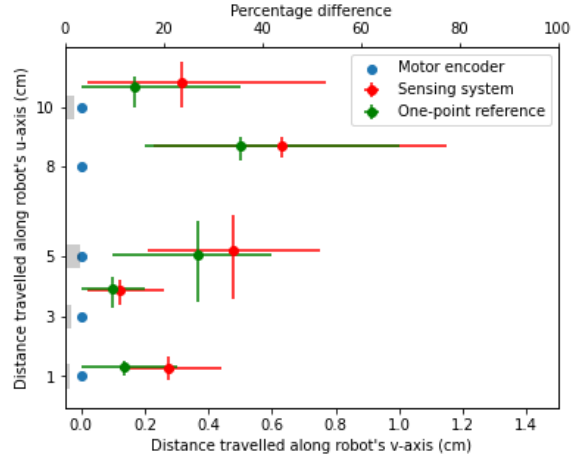
The visual system has two main objectives, calculate relative angle, and relative distance between the follower robot and its beacon neighbour.

5 Algorithms

The leader robot is programmed to travel along its v-axis for a constant velocity per given timestep. The follower robot algorithm is shown in Fig. 9. The data collecting phase is requested for the velocity prediction algorithm. In data collecting phase, the predicted velocity of timestep $k + 1$ is the final velocity of timestep k . The follower robot algorithm has three sub-algorithms: the movement algorithm is responsible for executing the predicted velocity for each given



(a)



(b)

Figure 7: Travelled distance comparison. Various travelling distances are pre-set and converted into wheel rotations according to robot's individual motor calibration functions. Travelled distance measured by motor encoder, by sensing system, and by one-point reference method is in blue, red, and green, respectively. Gray bar represents the percentage difference of measured distance between sensing system and one-point reference method. (a) Travelling along v-axis. (b) Travelling along u-axis.

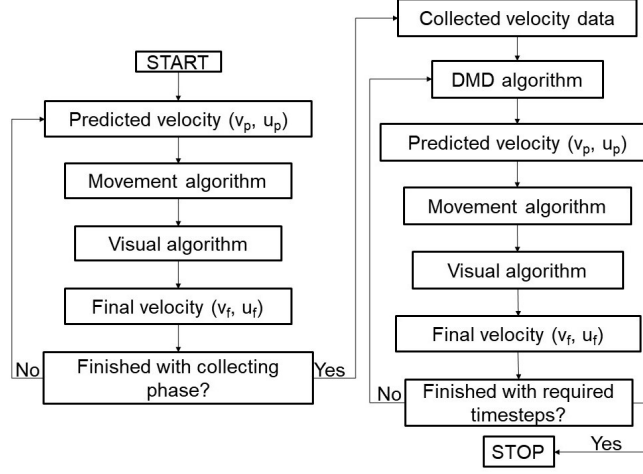


Figure 9: The overall algorithm scheme for follower robot. In the main algorithm, there is three sub-algorithm: movement algorithm, visual algorithm, and velocity prediction algorithm.

timesteps; the visual algorithm is responsible for correcting the relative position and angle of the follower robot to its beacon neighbour, since the velocity prediction has limited accuracy; the velocity prediction algorithm is responsible for velocity prection using data of previous velocities.

5.1 Movement algorithm

The movement algorithm converts predicted distance (x_p, y_p) to wheel rotations of movement along robot's u-axis and v-axis according to each robot's own motor calibration function presented in section 4.2.1. During each movement, external encoder measure and records the actual travelled distance.

5.2 Visual algorithm

Pixy2 detects color blocks and label them to its respective color signature. The final objective of the follower robot is to obtain a predefined relative position with respect to one-point reference, with zero relative angle to its beacon neighbour.

In order to understand Pixy2's behaviour with respect to relative position and angle, we set the beacon neighbour's position to be at the origin, $(0,0)$, and taking it as the reference point. 45 cm along u-axis, and ± 45 cm along v-axis relative distance between follower robot and its beacon neighbour are considered. Image data of Pixy2, including block color signature, block position, and block width and height, are captured for every 5 cm. When follower robot's v-axis is parallel to its beacon neighbour, it is considered to have zero relative

angle. The relative angle become positive in clockwise direction of the follower robot, taking the beacon neighbour as frame of reference. For each position, nine different relative angle, $\pm 60^\circ, \pm 45^\circ, \pm 30^\circ, \pm 15^\circ, 0^\circ$ are also considered. For specific parameter of Pixy2 see section C.

Based on Fig. 10, which is the overlaid image data of all relative angles, we define four areas. The unattainable area in red represent the positions where the follower robot is not allowed due to the volume of robots. The Front area in green, where the follower robot will always capture at least the front color signature block. The Target area in blue, where the follower robot only capture the Target color signature block. The Rear area in yellow, where the follower robot will always capture at least the Rear color signature block. The visual algorithm uses image data of Pixy2 to decided movements taking by the follower robot. It is designed to guide the follower robot to first attain Target area, then finetune its relative position and angle to obtain the final position.

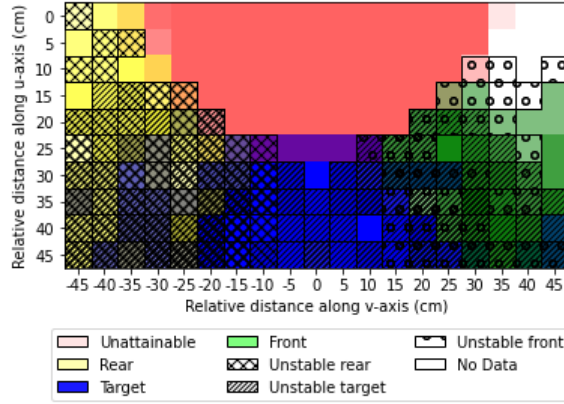


Figure 10: Pixy2 captured images with respect to relative position. All relative angles are overlaid. The overlap between unattainable area and other areas are due to different relative angles. This overlap do not affects the design of the visual algorithm.

To briefly summarize the visual algorithm for attaining Target area, the follower robot first checks the number of blocks it has detected. Four different cases are consider: for both one and two blocks, the follower robot will proceed to check the color signature of the detected blocks and perform movements along u-axis and v-axis according to different color signature; for more than two blocks, the follower robot would move along u-axis and get away from its beacon neighbour; for zero block, the follower robot would simply stop. Fig. 11 (in red background) shows the detailed algorithm flow for attaining the Target area. Notice that all movement in the algorithm is taking robot itself as frame of reference.

After the follower robot attains Target area, movement with finetuning is required. Shown in Fig. 11 (in blue background), Target color signature block's

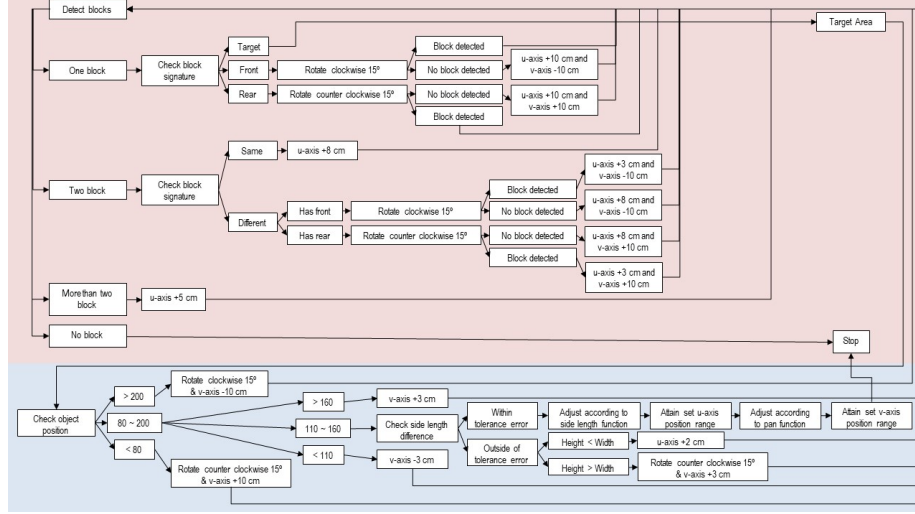


Figure 11: Visual algorithm flow for entering Target area in purple. Visual algorithm flow for obtaining ideal position while in Target area in red.

position, width, and height are used for the finetuning process. We first adjust the position of the Target color signature block, that is the relative position between follower robot and its beacon neighbour along v-axis (Fig. 12), then adjust the distance along u-axis (Fig. 13).

Since when adjusting position along v-axis, the follower robot do not have information about its relative position along u-axis, we finetune along v-axis in the range of $(-3, 3)$, where the difference in pan functions between various u-axis distance is small. The finetuning process tolerants error (section D) for color signature block's side length difference, u-axis position and v-axis position due to unavoidable flickering of the Pixy2 image.

5.3 Velocity prediction algorithm

To stay in lattice formation as the robots travelling through external potential, individual robot needs dynamic control of its trajectory. The visual system only provided limited sensing area for the follower robot to adjust its position and angle. To be able to track its beacon neighbour with higher accuracy and efficiency, a velocity prediction algorithm is requested for the follower robot.

5.3.1 Koopman operator theory and Online Dynamic Mode Decomposition

In the experiment, we consider the robot's trajectory to be a discrete-time dynamical system,

$$\mathbf{x}_{k+1} = \mathbf{F}(\mathbf{x}_k), \quad (4)$$

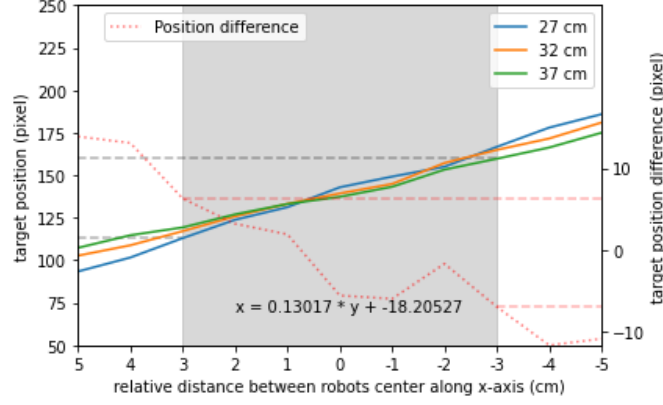


Figure 12: Relative distance along v-axis verse Pixy2 Target color signature block position function. Blue, orange, and green lines represent different relative distance between robots along u-axis. The red dotted line represents the maximum difference in Pixy2 Target color signature block position for various relative distance along u-axis. Gray area, $(-3, 3)$ cm represent finetuning area. Inside the finetuning area, the maximum difference in Pixy2 Target color signature block position for various relative distance along u-axis is less than 7 pixels. The finetuning area corresponds to Pixy2 Target color signature block position range 110 – 160, shown in horizontal dotted gray lines.

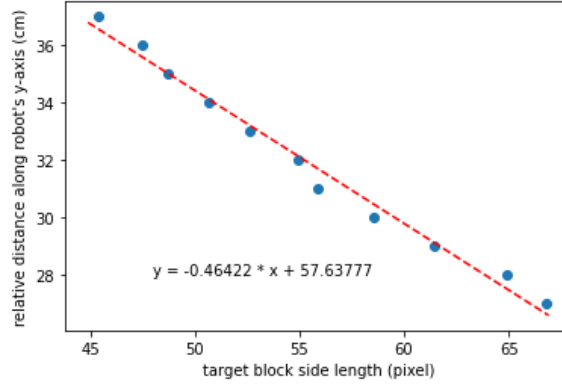


Figure 13: Target block side length verses relative distance along u-axis with zero relative distance along v-axis and zero relative angle.

where \mathbf{x}_k is the sampling of the state of the system, that is the position of the robot, in discrete given timesteps Δt , and \mathbf{F} is a vector field depends on the system. Due to the curvature property of the external potential manifold, the trajectories of robots are essentially nonlinear. To analyze nonlinear dynamic

with linear technique, we utilize Koopman operator theory and Dynamic Mode Decomposition.

Koopman theory has proved the possibility of representing a nonlinear dynamical system in terms of an infinite-dimensional linear operator acting on a Hilbert space of measurement functions of the state of the system. The basic elements of Koopman spectral analysis is discussed in [4, 22, 32]. For systems with unknown governing equation, such as in our situation, Dynamic Mode Decomposition (DMD) algorithm is adopted to find approximates of the Koopman operator [36, 39].

We consider a sequential set of data vectors $\{\mathbf{x}_0, \mathbf{x}_1, \dots, \mathbf{x}_m\}$, where each $\mathbf{x}_k \in \mathbb{R}^n$, are system states of time t_0 to t_m . These data can be arranged into two matrices

$$\mathbf{A} = \begin{bmatrix} | & | & & | \\ \mathbf{x}_0 & \mathbf{x}_1 & \dots & \mathbf{x}_{m-1} \\ | & | & & | \end{bmatrix}, \quad (5)$$

$$\mathbf{B} = \begin{bmatrix} | & | & & | \\ \mathbf{x}_1 & \mathbf{x}_2 & \dots & \mathbf{x}_m \\ | & | & & | \end{bmatrix}. \quad (6)$$

We assume there exist an operator \mathbf{T} that approximates the nonlinear dynamic of the system as

$$\mathbf{x}_{k+1} \approx \mathbf{T}\mathbf{x}_k. \quad (7)$$

Then the best-fit operator \mathbf{T} is defined as

$$\mathbf{T} = \arg \min_{\mathbf{T}} \|\mathbf{B} - \mathbf{T}\mathbf{A}\|_F, \quad (8)$$

where $\|\cdot\|_F$ is the Frobenius norm. The unique solution to least-square problem is given by

$$\mathbf{T} = \mathbf{B}\mathbf{A}^\dagger, \quad (9)$$

where \mathbf{A}^\dagger denotes the Moore-Penrose pseudoinverse of \mathbf{A} .

Online DMD algorithm updates operator \mathbf{T} for every timesteps, providing a more reliable operator \mathbf{T} for the prediction of future system states. The algorithm computes \mathbf{T}_{k+1} given \mathbf{T}_k and new pairs of data $(a_{k+1}, b_{k+1}) \equiv (x_k, x_{k+1})$, on the assumption that \mathbf{T}_{k+1} is close to \mathbf{T}_k in some sense.

5.3.2 Online DMD Algorithm

For the second phase, Online DMD algorithm shown below is used to prediction the velocity of the next timestep. For mathematical details, see section E.

Algorithm 1. (Online DMD)

1. Arrange the collected velocities x_k at each given timesteps into two matrices

$$\begin{aligned}\mathbf{A} &\equiv [x_0 \ x_1 \ x_2], \\ \mathbf{B} &\equiv [x_1 \ x_2 \ x_3].\end{aligned}$$

2. Compute \mathbf{T}_k and $(\mathbf{A}_k \mathbf{A}_k^T)^{-1}$.
3. Predict \mathbf{b}_{k+1} .
4. Correcting \mathbf{b}_{k+1} by visual algorithm.
5. Update \mathbf{T}_k and $(\mathbf{A}_k \mathbf{A}_k^T)^{-1}$ using corrected data pair $(\mathbf{a}_{k+1}, \mathbf{b}_{k+1})$.

6 Experiment and Discussion

6.1 Experimental results

For the experiment, one leader robot and one follower robot is used. The leader robot is set to travel 5 cm for each given timesteps. The follower robot initial velocity is the same as the leader robot, and it uses the algorithm described in section 5.

Two tracks are chosen. Track one runs horizontally on the external potential, with 15 timesteps, while track two runs diagonally with 20 timesteps. The initial position of the leader robot is predefined, while the follower robot is placed at 32 cm away in the v-axis, 0 cm in the u-axis, with zero angle, relative to the leader robot. Camera is located above the center point of the external potential, and photos are taken for each movement of the robots to obtain their trajectories. For both track, two types of algorithm is used. Figs. 14 (a) and (c) use DMD algorithm to predict next timestep velocity, while Figs. 14 (b) and (d) only use the velocity one-timestep before for velocity prediction, and is named non-DMD velocity prediction.

Overall, the follower robot's algorithm is succesful in tracking the leader robot for both track. Even though for track two without using DMD prediction algorithm, the follower robot lost the sight of the leader robot at last timestep. The visual algorithm shows its ability in correcting the relative position and angles when prediction is not ideal (at timestep 14).

To examine the difference between follower robot's algorithm with DMD prediction and without DMD prediction, the correction distance in the visual algorithm stage is compared as shown in Fig. 15. In total, the correction distance of follower robot's algorithm with DMD prediction is 147% of algorithm without DMD prediction for track one, and 22% for track two.

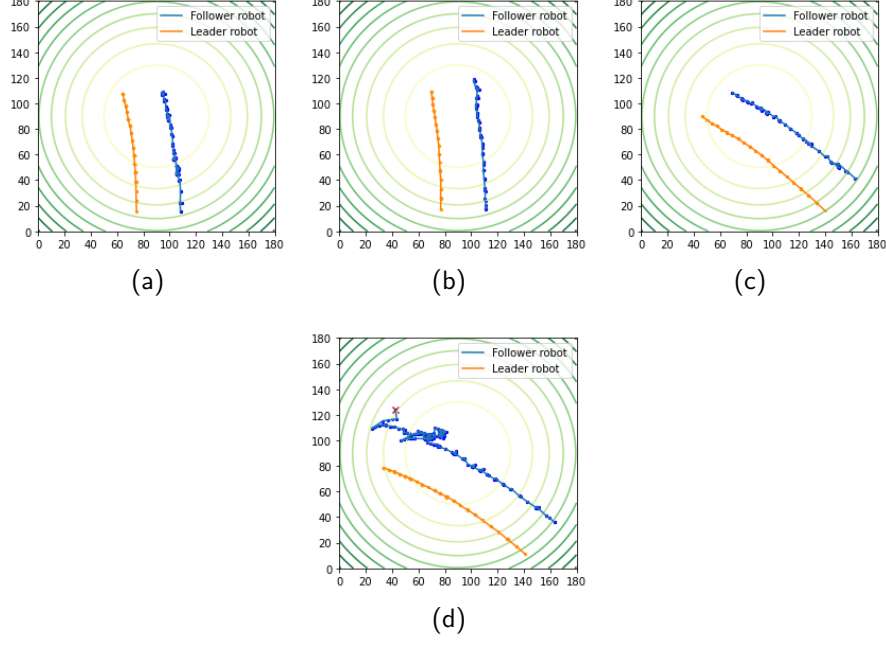
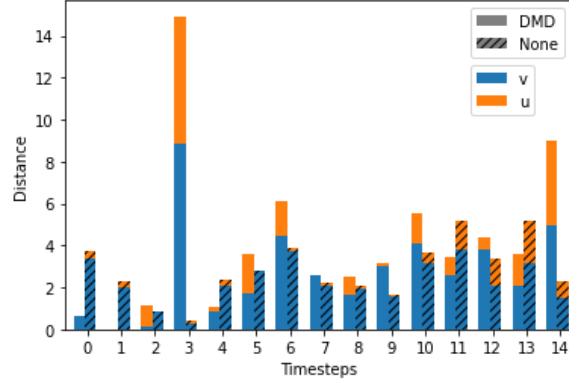


Figure 14: Trajectory of the leader robot and follower robot in external potential. The trajectory of leader robot is in orange, the trajectory of follower robot is in blue. The green contour line in the background represents the external potential. All robots have initial velocity 5 cm per given timestep. Red cross mark indicates that the follower robot have lost the visual of its beacon neighbour (the leader robot). (a) Track one with DMD velocity prediction algorithm. Initial position of the leader robot is at (76.3, 15.8) cm. Error due to camera distortion is at maximum of 1.3 cm. (b) Track one without DMD velocity prediction algorithm. Initial position of the leader robot is (76.9, 17.3) cm. Error due to camera distortion is at maximum of 1.7 cm. (c) Track two with DMD velocity prediction algorithm. Initial position of the leader robot is (141.2, 11.1) cm. Error due to camera distortion is at maximum of 1.7 cm. (d) Track two without DMD velocity prediction algorithm. Initial position of the leader robot is (139.7, 16.3) cm. Error due to camera distortion is at maximum of 2.7 cm.

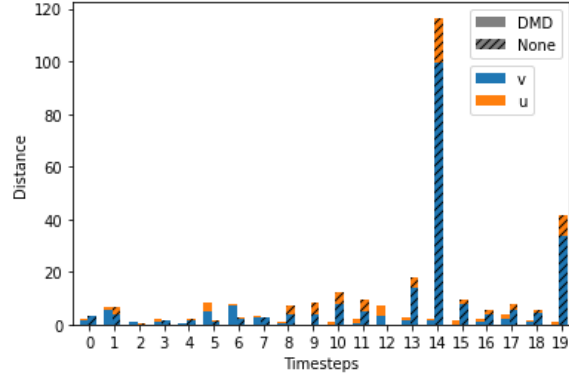
6.2 Discussion

6.2.1 On DMD prediction algorithm

Online DMD algorithm used for velocity prediction assumes there is a linear operator advances some measurement functions (velocity) the nonlinear system state (trajectory of the follower robot). To find this linear operator, least-square estimation is used. This implies, in the experiment, the nonlinearity of the trajectory of the leader robot would affect the accuracy of the velocity prediction



(a)



(b)

Figure 15: Correction distance comparison between DMD prediction algorithm and Non-DMD prediction algorithm for (a) track one and (b) track two. For each timestep, distance travelled in v-axis (blue) and u-axis (orange) of robot are recorded for both DMD prediction and Non-DMD prediction algorithm (striped).

algorithm. For track one, the external potential mainly affects movement along v-axis. Also, due to the symmetry of the external potential, this effect along v-axis is similar for both leader and follower robot. Therefore, since the predefined velocity for the leader robot is constant, the trajectory of the follower robot is close to linear. For track two, the leader robot trajectory and follower robot trajectory are in different region of the external potential, thus the effects of curvature differs. Due to the curvature of the external potential, trajectory of the follower robot in track two is more nonlinear than track one. This difference in trajectory nonlinearity explain the discrepancy in DMD velocity prediction effectiveness for track one and two.

6.2.2 On limitations

One of the issues we intend to address with the current experiment is to identify its limitations and possible improvements which could be made.

Mobility Due its own weight, the robot is difficult in excuting an accurate velocity per given timestep for region of the external potential where the curvature is larger. This under-performance would affects both visual algorithm for positioning correction and velocity prediction algorithm. Decrease the overall weight and adding PID control to the robot might improve on the robot's mobility performance.

Communication delay For the experiment in this paper, the leader robot have waited for the follower robot to obtain desire position before moving for each given timesteps. This waiting time would increase as the swarm increases scale.

Visual system error The visual system uses Pixy2 for image recognition. Pixy2's sensitivity directly affects the accuracy of visual algorithm. The visual algorithm used in the experiment requires high sensitivity, which unavoidably leads to image data reading error due to flickering. Other sensing method could be considered for future works.

7 Conclusion

This paper presented experimental results on realizing defined lattice formation in nonlinear external potential using mobile robots. Two omnidirectional mobile robots are design and experimented in nonlinear two-dimensional elliptic paraboloid external potential. The formation control algorithm for the follower robot includes velocity prediction algorithm by DMD, visual algorithm for position correction, and movement algorithm for robot's mobility. The algorithm is successful in maintaining the desired formation, and is easily scalable.

Algorithm with DMD velocity prediction decreases the work load for position correction by visual algorithm, which in term increases the efficiency of the overall formation control. However, DMD velocity prediction algorithm out performs algorithm without DMD prediction if the trajectory of the follower robot is nonlinear, while no significant difference for trajectory that is close to linear.

Improvements can be made on the mobility and visual system of the robot to increase its performance. We envisage a larger lattice formation to be experimented on the nonlinear external potential, and the formation analysis algorithm in [36] can be verified in experiment for future work.

Acknowledgments

Y.W and T.H acknowledges Professor H. Arai and N. Satoh from Chiba Institute of Technology for helpful discussions. Y.W is supported by the Japanese Government MEXT Scholarship Program.

8 References

References

- [1] Alessandro Attanasi, Andrea Cavagna, Lorenzo Del Castello, Irene Giardina, Tomas S. Grigera, Asja Jelić, Stefania Melillo, Leonardo Parisi, Oliver Pohl, Edward Shen, and Massimiliano Viale. Information transfer and behavioural inertia in starling flocks. *Nature Physics*, 10(9):691–696, 2014.
- [2] T. Balch and R.C. Arkin. Behavior-based formation control for multirobot teams. *IEEE Transactions on Robotics and Automation*, 14(6):926–939, 1998.
- [3] Florian Berlinger, Melvin Gauci, and Radhika Nagpal. Implicit coordination for 3d underwater collective behaviors in a fish-inspired robot swarm. *Science Robotics*, 6(50):eabd8668, 2021.
- [4] S.L. Brunton and J.N. Kutz. *Data-Driven Science and Engineering: Machine Learning, Dynamical Systems, and Control*. Cambridge University Press, Cambridge, England, 2019.
- [5] Chien Chern Cheah, Saing Paul Hou, and Jean Jacques E. Slotine. Region-based shape control for a swarm of robots. *Automatica*, 45(10):2406–2411, 2009.
- [6] Jianing Chen, Melvin Gauci, Wei Li, Andreas Kolling, and Roderich Groß. Occlusion-based cooperative transport with a swarm of miniature mobile robots. *IEEE Transactions on Robotics*, 31(2):307–321, 2015.
- [7] A.K. Das, R. Fierro, V. Kumar, J.P. Ostrowski, J. Spletzer, and C.J. Taylor. A vision-based formation control framework. *IEEE Transactions on Robotics and Automation*, 18(5):813–825, 2002.
- [8] Olaf Diegel, Aparna Badve, Glen Bright, Johan Potgieter, and Tlale Sylvester. Improved mecanum wheel design for omni-directional robots. In *2002 Australasian Conference on Robotics and Automation*, pages 117–121, 2002.
- [9] J. Fredslund and M.J. Mataric. A general algorithm for robot formations using local sensing and minimal communication. *IEEE Transactions on Robotics and Automation*, 18(5):837–846, 2002.

- [10] Veysel Gazi and Barış Fidan. Coordination and control of multi-agent dynamic systems: models and approaches, 2006.
- [11] Vladimir G. Ivancevic and Tijana T. Ivancevic. *Applied Differential Geometry: A Modern Introduction*. World Scientific Publishing Co. Pte. Ltd., Singapore, 2007.
- [12] Arthur Kahn, Julien Marzat, and Hélène Piet-Lahanier. Formation flying control via elliptical virtual structure. In *2013 10th IEEE INTERNATIONAL CONFERENCE ON NETWORKING, SENSING AND CONTROL (ICNSC)*, pages 158–163, 2013.
- [13] Gal A. Kaminka and Inna Frenkel. Towards flexible teamwork in behavior-based robots: Extended abstract. In *Proceedings of the Fourth International Joint Conference on Autonomous Agents and Multiagent Systems, AAMAS '05*, page 1355–1356, New York, NY, USA, 2005. Association for Computing Machinery.
- [14] Sanza T. Kazadi. *Swarm engineering*. Dissertation (ph.d.), California Institute of Technology, 2000.
- [15] Hung Manh La and Weihua Sheng. Distributed sensor fusion for scalar field mapping using mobile sensor networks. *IEEE Transactions on Cybernetics*, 43(2):766–778, 2013.
- [16] Emmett Lalish, Kristi A. Morgansen, and Takashi Tsukamaki. Formation tracking control using virtual structures and deconfliction. In *Proceedings of the 45th IEEE Conference on Decision and Control*, pages 5699–5705, 2006.
- [17] John M. Lee. *Riemannian Manifolds: An Introduction to Curvature*. Springer-Verlag New York, Inc., New York, USA, 1997.
- [18] Norman H. M. Li and Hugh H. T. Liu. Formation uav flight control using virtual structure and motion synchronization. In *2008 American Control Conference*, pages 1782–1787, 2008.
- [19] Ugo Lopez, Jacques Gautrais, Iain D. Couzin, and Guy Theraulaz. From behavioural analyses to models of collective motion in fish schools. *Interface Focus*, 2(6):693–707, 2012.
- [20] Ali Marjovi and Lino Marques. Optimal swarm formation for odor plume finding. *IEEE Transactions on Cybernetics*, 44(12):2302–2315, 2014.
- [21] David Mateo, Nikolaj Horsevad, Vahid Hassani, Mohammadreza Chamanbaz, and Roland Bouffanais. Optimal network topology for responsive collective behavior. *Science Advances*, 5(4):eaau0999, 2019.
- [22] Alexandre Mauroy, Igor Mezic, and Yoshihiko (Eds.) Susuki. *The Koopman Operator in Systems and Control Concepts, Methodologies, and Applications: Concepts, Methodologies, and Applications*. 01 2020.

- [23] K. N. McGuire, C. De Wagter, K. Tuyls, H. J. Kappen, and G. C. H. E. de Croon. Minimal navigation solution for a swarm of tiny flying robots to explore an unknown environment. *Science Robotics*, 4(35):eaaw9710, 2019.
- [24] Reza Olfati-Saber. Flocking for multi-agent dynamic systems: algorithms and theory. *IEEE Transactions on Automatic Control*, 51:401–420, 2006.
- [25] Rattanachai Ramaithitima, Michael Whitzer, Subhrajit Bhattacharya, and Vijay Kumar. Automated creation of topological maps in unknown environments using a swarm of resource-constrained robots. *IEEE Robotics and Automation Letters*, 1(2):746–753, 2016.
- [26] Wei Ren and Randal W. Beard. Decentralized scheme for spacecraft formation flying via the virtual structure approach. *Journal of Guidance Control and Dynamics*, 27:73–82, 2004.
- [27] Craig W. Reynolds. Flocks, herds and schools: A distributed behavioral model. In *Proceedings of the 14th Annual Conference on Computer Graphics and Interactive Techniques*, SIGGRAPH '87, page 25–34, New York, NY, USA, 1987. Association for Computing Machinery.
- [28] Joan Saez-Pons, Lyuba Alboul, Jacques Penders, and Leo Nomdedeu. Multi-robot team formation control in the guardians project. *Industrial Robot: An International Journal*, 2010.
- [29] Jinyan Shao, Guangming Xie, Junzhi Yu, and Long Wang. Leader-following formation control of multiple mobile robots. In *Proceedings of the 2005 IEEE International Symposium on, Mediterrean Conference on Control and Automation Intelligent Control, 2005.*, pages 808–813, 2005.
- [30] Procópio Stein, Anne Spalanzani, Vítor Santos, and Christian Laugier. Leader following: A study on classification and selection. *Robotics and Autonomous Systems*, 75:79–95, 2016. Assistance and Service Robotics in a Human Environment.
- [31] Dali Sun, Alexander Kleiner, and Bernhard Nebel. Behavior-based multi-robot collision avoidance. In *2014 IEEE International Conference on Robotics and Automation (ICRA)*, pages 1668–1673, 2014.
- [32] Yoshihiko Susuki, Igor Mezic, Fredrik Raak, and Takashi Hikiyara. Applied koopman operator theory for power systems technology. *Nonlinear Theory and Its Applications, IEICE*, 7(4):430–459, 2016.
- [33] Kar-Han Tan and M.A. Lewis. Virtual structures for high-precision cooperative mobile robotic control. In *Proceedings of IEEE/RSJ International Conference on Intelligent Robots and Systems. IROS '96*, volume 1, pages 132–139 vol.1, 1996.

- [34] Ali Emre Turgut, Hande Çelikkanat, Fatih Gökçe, and Erol Sahin. Self-organized flocking in mobile robot swarms. *Swarm Intelligence*, 2:97–120, 2008.
- [35] Tamás Vicsek and Anna Zafeiris. Collective motion. *Physics Reports*, 517(3):71–140, 2012.
- [36] Yanran Wang and Takashi Hikiyara. Two-dimensional swarm formation in time-invariant external potential: Modeling, analysis, and control. *Chaos: An Interdisciplinary Journal of Nonlinear Science*, 30(9):093145, 2020.
- [37] Dongdong Xu, Xingnan Zhang, Zhangqing Zhu, Chunlin Chen, and Pei Yang. Behavior-based formation control of swarm robots. *Mathematical Problems in Engineering*, 2014:1–13, 2014.
- [38] Toshiyuki Yasuda, Akitoshi Adachi, and Kazuhiro Ohkura. Self-organized flocking of a mobile robot swarm by topological distance-based interactions. In *2014 IEEE/SICE International Symposium on System Integration*, pages 106–111, 2014.
- [39] Hao Zhang, C.W. Rowley, E.A. Deem, and L.N. Cattafesta. Online dynamic mode decomposition for time-varying systems. *SIAM Journal on Applied Dynamical Systems*, 18(3):1586–1609, 2019.
- [40] Siwei Zhang, Robert Pöhlmann, Thomas Wiedemann, Armin Dammann, Henk Wymeersch, and Peter Adam Hoeher. Self-aware swarm navigation in autonomous exploration missions. *Proceedings of the IEEE*, 108(7):1168–1195, 2020.

A Differential geomtry

Let $U \subseteq \mathbb{R}^n$ be a non-empty open subset and $F : U \rightarrow \mathbb{R}$ a C^∞ function defining the external potential. Let $M \subseteq U \times \mathbb{R}$ be the graph of f . The closed subset M in $U \times \mathbb{R}$ projects homeomorphically onto U with inverse $(x_1, \dots, x_n) \mapsto (x_1, \dots, x_n, F(x_1, \dots, x_n))$ that is a smooth mapping from U to $U \times \mathbb{R}$. M is a closed smooth submanifold of $U \times \mathbb{R}$. Using the standard Riemannian metric on $U \times \mathbb{R} \subseteq \mathbb{R}^{n+1}$, the induced metric g on M at a point $p \in M$ is

$$g(p) = \langle \partial_{q_i}|_p, \partial_{q_j}|_p \rangle_p dq_i(p) \otimes dq_j(p) \quad (10)$$

with coordinate chart $\{q_i\}$ on M . Each $\partial_{q_i}|_p \in T_p M$ can be represented as a linear combination of $\{\partial_{x_i}|_p\} \in T_p(\mathbb{R}^{n+1})$, given as

$$\partial_{q_i}|_p = \partial_{x_i}|_p + \partial_{x_i} f(p) \partial_{x_{n+1}}|_p. \quad (11)$$

Consider the aforementioned graph M as a C^∞ Riemannian manifold. Given a curve, $C : [a, b] \rightarrow M$, a *vector field* X along C is any section of the tangent bundle TM over C ($X : [a, b] \rightarrow TM$, projection $\pi : TM \rightarrow M$, such that $\pi \circ X = C$). If M is a smooth manifold, all vector field on the manifold are also smooth. We denote the collection of all smooth vector fields on manifold M as $\mathfrak{X}(M)$. For a Riemannian manifold (M, g) , the *Levi-Civita connection* ∇_g on M is the unique connection on TM that has both metric compatibility and torsion freeness. The Christoffel symbols of the second kind are the connection coefficients (in a local chart) of the Levi-Civita connection denoted as

$$\Gamma^a_{bc} = \frac{1}{2} g^{ad} (\partial_c g_{db} + \partial_b g_{dc} - \partial_d g_{bc}). \quad (12)$$

For a Riemannian manifold (M, g) , a curve is called *geodesic* with respect to the connection ∇_g if its acceleration is zero. That is a curve γ where $\nabla_{\dot{\gamma}} \dot{\gamma} = 0$. A geodesic curve in n -dimensional Riemannian manifold can be expressed as a system of second order ordinary differential equations,

$$\frac{d^2 \gamma^\lambda}{dt^2} + \Gamma^\lambda_{\mu\nu} \frac{d\gamma^\mu}{dt} \frac{d\gamma^\nu}{dt} = 0. \quad (13)$$

All geodesics are the shortest path between any two points on the manifold.

B External potential specification

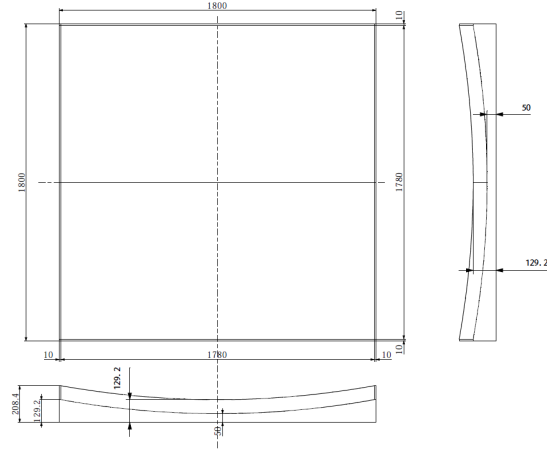


Figure 16: Specification of external potential. All units in mm.

C Pixy2 parameters

Table 1: Pixy2 paramter settings

Parameter names	Values
Target signature range	5.0
Front signature range	6.0
Rear signature range	6.0
Camera brightness	100
Block filtering	40
Max merge distance	4
Min block area	20
Signature teach threshold	5600
LED brightness	4960
Auto exposure correction	On
Auto white balance	On
Flicker avoidance	On
Mininum frames per second	30

D Pixy2 error

Table 2: Pixy2 error tolerance for visual algorithm

Data names	Tolerance values
Side length difference	4 pixel
v-axis position	5 pixel
u-axis position	1.5 cm

E Online Dynamic Mode Decomposition

Using (9) in Section 5, we have

$$\mathbf{T}_k = \mathbf{B}_k \mathbf{A}_k^T (\mathbf{A}_k \mathbf{A}_k^T)^{-1}. \quad (14)$$

We define two new matrices \mathbf{P}_k and \mathbf{Q}_k ,

$$\mathbf{Q}_k = \mathbf{B}_k \mathbf{A}_k^T, \quad (15)$$

$$\mathbf{P}_k = (\mathbf{A}_k \mathbf{A}_k^T)^{-1}, \quad (16)$$

so that $\mathbf{T}_k = \mathbf{Q}_k \mathbf{P}_k$. \mathbf{P}_k is well-defined if we ensure $\mathbf{A}_k \mathbf{A}_k^T$ is invertible. The operator \mathbf{T} at time t_{k+1} is related to \mathbf{T}_k as

$$\begin{aligned} \mathbf{T}_{k+1} &= \mathbf{Q}_{k+1} \mathbf{P}_{k+1} \\ &= (\mathbf{Q}_k + \mathbf{b}_{k+1} \mathbf{a}_{k+1}^T) (\mathbf{P}_k^{-1} + \mathbf{a}_{k+1} \mathbf{a}_{k+1}^T)^{-1}. \end{aligned} \quad (17)$$

Using Sherman-Morrison formula, we can express \mathbf{P}_{k+1} as

$$\begin{aligned} \mathbf{P}_{k+1} &= (\mathbf{P}_k^{-1} + \mathbf{a}_{k+1} \mathbf{a}_{k+1}^T)^{-1} \\ &= \mathbf{P}_k - \frac{\mathbf{P}_k \mathbf{a}_{k+1} \mathbf{a}_{k+1}^T \mathbf{P}_k}{1 + \mathbf{a}_{k+1}^T \mathbf{P}_k \mathbf{a}_{k+1}}. \end{aligned} \quad (18)$$

\mathbf{P}_{k+1} can be updated more efficiently, without the computation of inverses. Combining (18) and (17), we obtain the formula

$$\mathbf{T}_{k+1} = \mathbf{T}_k + \frac{(\mathbf{b}_{k+1} - \mathbf{T}_k \mathbf{a}_{k+1}) \mathbf{a}_{k+1}^T \mathbf{P}_k}{1 + \mathbf{a}_{k+1}^T \mathbf{P}_k \mathbf{b}_{k+1}}. \quad (19)$$

\mathbf{T}_{k+1} is computed using \mathbf{T}_k and new data pair $\{\mathbf{a}_{k+1}, \mathbf{b}_{k+1}\}$.